Gas around galaxy haloes – II. Hydrogen absorption signatures from the environments of galaxies at redshifts 2 < z < 3

Avery Meiksin,[1][*] James S. Bolton[2] and Eric R. Tittley[1]

[1]*SUPA[†], Institute for Astronomy, University of Edinburgh, Blackford Hill, Edinburgh EH9 3HJ, UK*
[2]*School of Physics and Astronomy, University of Nottingham, University Park, Nottingham NG7 2RD, UK*

ABSTRACT

We compare predictions of large-scale cosmological hydrodynamical simulations for neutral hydrogen absorption signatures in the vicinity of 10^{11}–$10^{12.5}$ $M_\odot$ haloes with observational measurements. Two different hydrodynamical techniques and a variety of prescriptions for gas removal in high-density regions are examined. Star formation and wind feedback play only secondary roles in the H I absorption signatures outside the virial radius, but play important roles within. Accordingly, we identify three distinct gaseous regions around a halo: the virialized region, the mesogalactic medium outside the virial radius arising from the extended haloes of galaxies out to about two turnaround radii and the intergalactic medium beyond. Predictions for the amount of absorption from the mesogalactic and intergalactic media are robust across different methodologies, and the predictions agree with the amount of absorption observed around star-forming galaxies and quasi-stellar object host galaxies. Recovering the measured amount of absorption within the virialized region, however, requires either a higher dynamic range in the simulations, additional physics, or both.

Key words: galaxies: formation – intergalactic medium – quasars: absorption lines – large-scale structure of Universe.

1 INTRODUCTION

The environment of a forming galaxy is expected to be violent and complex. Cooling and accreting gas will be thermally unstable on multiple scales, leading to star formation. Supernova-driven winds from young massive stars will drive back accreting hot gas, and may promote the accretion of cool gas, enhancing the cooling by the injection of metal-enriched material. An active galactic nucleus (AGN), particularly in more massive galaxies, will produce jets that may drive gas further out, heat it and redistribute metal-enriched gas, while the compression of gas latitudinal to the jet may enhance star formation. The evolution will be occasionally punctuated by major mergers with other haloes.

Cosmological simulations have begun filling in the physical details of these processes. A picture is emerging of two modes of gas accretion, a 'hot mode' in galaxies sufficiently massive for most gas to shock heat to virial temperatures before the onset of gradual cooling and a 'cold mode' in galaxies in which much of the gas does not sustain high post-shock temperatures and instead flows in primarily as cool gas streams (Kay et al. 2000; Kereš et al. 2005; Dekel & Birnboim 2006; van de Voort et al. 2011), a scenario supported by theoretical arguments (Birnboim & Dekel 2003).

The cooling gas feeds star formation in the galaxies. Simulations, however, tend to overpredict the amount of stars formed. Supernovae have long been suspected of suppressing star formation in galaxies, from ellipticals (Larson 1974; Silk et al. 1986) to dwarfs (Dekel & Silk 1986), to bring the amount of stars formed into agreement with observations. This view has been backed by large-scale hydrodynamical simulations, strongly suggesting that supernova-driven wind feedback may regulate the star formation rate in galaxies (e.g. Kay et al. 2002; Schaye et al. 2010; Haas et al. 2013). AGN jets may furthermore regulate star formation in the more massive galaxies (e.g. van de Voort et al. 2011; Haas et al. 2013).

However, direct observational evidence for these mechanisms is scanty. While hydrogen and metal emission lines show evidence for winds in star-forming galaxies (SFGs) at redshifts $z > 1$ with velocities exceeding the escape velocities of the haloes (Weiner et al. 2009; Steidel et al. 2010; Genzel et al. 2011), the extent of the winds and their impact on the surrounding gas are still unknown. Maps of gas emission in active galaxies reveal winds extending over tens of kiloparsecs, but so far only at low redshifts (Harrison et al. 2014). Consequently, the search for cold streams in absorption in the spectra of background quasi-stellar objects (QSOs) or bright galaxies has attracted increasing recent attention. The availability of large QSO catalogues with a high sky density (e.g. Abazajian et al. 2009; Ahn et al. 2012) has presented an opportunity, along with follow-up spectroscopy, to study the gaseous environments of

SFGs and AGNs through absorption measurements with unprecedented detail. Observations of intergalactic H I show a rise in the H I optical depth near Lyman-break galaxies (LBGs; Steidel et al. 2010; Crighton et al. 2011; Rakic et al. 2012) and QSOs (Hennawi et al. 2006; Prochaska et al. 2013b), and thus evidence for extended cool gas surrounding galactic haloes.

Several galaxy formation simulations have sought to establish consistency with these data. Of particular focus have been absorbers optically thick at the photoelectric edge, Lyman limit systems (LLSs) and damped Lyα absorbers (DLAs). Simulations suggest that a large fraction of these absorption systems at $z > 2$ may be accounted for by cold-mode accretion of circumgalactic gas (Faucher-Giguère & Kereš 2011; Fumagalli et al. 2011; van de Voort et al. 2012; Shen et al. 2013). However, numerical models have been less successful at reproducing the observed absorption around QSOs relative to SFGs (but see recent work by Rahmati et al. 2015). While the covering fraction of optically thick systems of SFGs in simulations matches the observations within the errors, most previous simulation predictions fall short of the covering fractions measured around QSOs (Fumagalli et al. 2014; Faucher-Giguere et al. 2015). Agreement with the trend of increasing H I absorption with decreasing impact parameter is also reported for the SFG sample of Steidel et al. (2010) (Fumagalli et al. 2011; Goerdt et al. 2012; Shen et al. 2013), but for a sample of QSOs, simulations greatly underpredict the observed amount of absorption by circumgalactic gas (Prochaska et al. 2013b).

In this paper, we examine the H I absorption around galaxy haloes in large-scale cosmological hydrodynamical simulations, by considering both the circumgalactic gas and the extended region surrounding it as it merges into the intergalactic medium (IGM). Previous simulations of the circumgalactic medium (CGM), generally defined as gas within 300 kpc (proper) of a galaxy, have instead typically been zoom-in models focused on the immediate surroundings of a galaxy, extending out to at most a few virial radii (e.g. Faucher-Giguère & Kereš 2011; Goerdt et al. 2012; Fumagalli et al. 2011, 2014; Faucher-Giguere et al. 2015). They have not therefore been able to fully exploit the growing amount of data probing the gas around galaxies to distances of several comoving megaparsecs. Recent absorption line studies have exploited large-box simulations, such as those of the OverWhelmingly Large Simulations (OWLS; Schaye et al. 2010), Illustris simulation (Vogelsberger et al. 2014) and EAGLE simulation (Schaye et al. 2015) projects. Applications to the IGM include constraints on the masses of the SFG haloes in the Keck Baryonic Structure Survey using the median Lyα optical depth measurements of Rakic et al. (2012, 2013), comparisons between the measured and predicted cross-correlation function between Lyα absorption and LBGs (Tummuangpak et al. 2014), and a very recent study by Rahmati et al. (2015) using the EAGLE simulations.

The analysis presented here is based on the ENZO and GADGET-3 simulations described in Meiksin, Bolton & Tittley (2014, hereafter Paper I). These are of sufficiently high resolution and volume to recover the hydrogen absorption properties of the IGM. In Paper I, we demonstrated that these IGM simulations make consistent predictions for the intergalactic gas properties beyond the halo turnaround radii, despite their differing numerical algorithms. However, the gas properties on smaller scales are highly dependent on star formation and feedback implementations (see also Nelson et al. 2015; Suresh et al. 2015). We shall use these simulations to construct spectra to examine how well the models match the observed statistics of H I absorption around galaxies and QSOs. We differ from previous work, however, by first taking a step back and asking whether the

absorption signatures of gas around galaxies show any evidence for star formation even without feedback. We then seek to establish the physical extent of excess hydrogen absorption over the contribution from the diffuse IGM around galaxies. We finally ask what observational evidence hydrogen absorption signatures provide for wind feedback in addition to star formation. We shall show that the strongest evidence for star formation arises from the gas within the virial radius. Excess integrated H I absorption from the large-scale IGM is found over an extended 'mesogalactic region', between the virial radius of the haloes and about twice the turnaround radius of the gas. The simulation results for the integrated absorption through this region agree well with measurements, and show little sensitivity to the presence of star formation or feedback. The region thus appears to be robustly described within the framework of Λ cold dark matter (ΛCDM) cosmologies with minimal additional physical assumptions.

This paper is organized as follows. In Section 2 we summarize the numerical simulations used in this work. The resulting H I optical depths and covering fractions around haloes are presented in Section 3, and these results are discussed in detail in Section 4. We present our conclusions in Section 5, and simulation convergence tests are discussed in Appendix A. All results are for a flat ΛCDM universe with the cosmological parameters $\Omega_m = 0.28$, $\Omega_b h^2 = 0.0225$ and $h = H_0/100 \, \text{km s}^{-1} \, \text{Mpc}^{-1} = 0.70$, representing the present-day total mass density, baryon density and Hubble constant, respectively. The power spectrum has spectral index $n_s = 0.96$, and is normalized to $\sigma_8 = 0.82$, consistent with the 9-year *Wilkinson Microwave Anisotropy Probe* data (Hinshaw et al. 2013). All distances are comoving unless stated otherwise.

2 NUMERICAL SIMULATIONS

2.1 Cosmological hydrodynamics codes

The numerical simulations are performed using ENZO, v.2 (Bryan et al. 2014), and GADGET-3, an updated version of the publicly available code GADGET-2 (last described by Springel 2005). The runs are summarized in Table 1, and further details may also be found in Paper I. As we focus on high-redshift haloes in this work, all the runs were stopped at $z = 2$. The Eulerian ENZO simulations were performed on the top-level grid only. One simulation uses 512^3 mesh zones and 512^3 CDM particles in a box 30 Mpc (comoving) on a side (E30_512), and the second one has 1024^3 mesh zones and 1024^3 CDM particles in a 60 Mpc box (E60_1024). The grid zones have a comoving width of 58.6 kpc. Since ENZO uses the particle-mesh method, the force resolution is limited to about five grid zones (Lukić et al. 2015), adequate for resolving the Jeans length of the photoionized gas. The smoothed particle hydrodynamics simulations performed with GADGET-3 were run with 512^3 CDM particles and 512^3 gas particles in a box 30 Mpc (comoving) along a side, with a force softening scale of 1.4 kpc (comoving). The baryonic and dark matter particle masses are 1.3×10^6 and $6.4 \times 10^6 \, \text{M}_\odot$, respectively.

No gas is removed from the ENZO simulations, producing a 'no star formation' control sample. However, because of the high densities and temperatures reached in the Lagrangian GADGET-3 simulations, gas must be removed in rapidly cooling regions. We adopt the star formation prescription of Springel & Hernquist (2003, hereafter SH03) in one model (G30sfnw), and include their supernova feedback prescription with a wind velocity of 484 km s^{-1} in another (G30sfw). Note, however, that any conclusions drawn

Table 1. Summary of the simulations performed in this work. The columns, from left to right, list the simulation name, the box size in comoving Mpc, the number of resolution elements in the simulation, the code used for the run, the star formation prescription and whether or not the model includes supernova-driven winds.

Name	Box size (Mpc)	Resolution elements	Method	Star formation	Winds
G30qLyα	30	2×512^3	GADGET-3	qLyα	N
G30sfnw	30	2×512^3	GADGET-3	SH03	N
G30sfw	30	2×512^3	GADGET-3	SH03	Y
E30_512	30	512^3	ENZO	None	N
E60_1024	60	1024^3	ENZO	None	N

from its use are exclusive to this particular algorithm (see also e.g. Dalla Vecchia & Schaye 2008). Indeed, absorption measurements like those we examine may provide a basis for discriminating between different feedback models. A comparison simulation, discussed in Appendix A, is also performed using the 'quick Lyα' method (G30qLyα), for which all gas cooler than 10^5 K and with an overdensity exceeding 1000 is converted into collisionless 'star' particles (without feedback). This is a computational trick used in IGM simulations to significantly speed up the computation (Viel, Haehnelt & Springel 2004). One disadvantage of the method is that it instantly converts clumps of dense cool gas into stars that may otherwise have survived as absorption systems. We use the method only as an alternative for testing the sensitivity of the results on the gas removal scheme. Except in Appendix A, all the GADGET-3 results presented here use the SH03 star formation prescription.

Both the ENZO and GADGET-3 codes solve the time-dependent ionization equations for hydrogen and helium. Photoionization, collisional ionization and radiative and dielectric recombinations are included. Thermal balance includes cooling by radiative and dielectric recombination, collisional ionization and excitation and thermal bremsstrahlung losses as well as Compton cooling off the cosmic microwave background. The codes adopt the photoionization and photoheating rates of Haardt & Madau (2012), except we adjusted the photoionization heating rate of singly ionized helium to reproduce the evolution of the IGM temperature in Becker et al. (2011) for $\gamma = 1.3$. The codes used identical atomic rates for the heating and cooling, as summarized in Meiksin (2009), except for adopting the H I electron excitation and collisional cooling rate of Scholz & Walters (1991). We have not included any photoionization from the central galaxies or QSOs, which could reduce the amount of absorption from high column density systems (Miralda-Escudé 2005; Schaye 2006). However, to date there is no firm evidence for a widespread transverse proximity effect from either SFGs or QSOs (Croft 2004; Kirkman & Tytler 2008). We also do not include the self-shielding of H I absorbers in our main analysis, although in Appendix A we show this has only a small effect on the integrated absorption statistics examined here. We include self-shielding corrections when discussing discrete absorption systems. Self-shielding will play an important role in the statistics of absorption systems optically thick at the Lyman edge, a point we discuss further in Appendix A. The role will be particularly important for damped systems, with $N_{H I} > 10^{19}$ cm^{-2}, since the photoelectric heating of the interior of these systems will be negligible. Their interiors will therefore be much cooler than given by the simulations, with a consequent hydrodynamical restructuring beyond the ability of any simple self-shielding correction to re-

cover. Full self-consistent radiative hydrodynamical computations are required, which are beyond the scope of this work.

2.2 Extraction of Lyα absorption statistics

The Lyα absorption spectra are computed at rest-frame velocity v along a line of sight through a periodic box of comoving side L as $\exp[-\tau_\alpha(v)]$, where

$$\tau_\alpha(v) = \frac{\sigma_\alpha \lambda_\alpha}{\pi^{1/2}} \frac{L}{1+z} \int dx\, n_{H I}(x) b(x)^{-1} e^{-(v-v_{los})^2/b^2}. \tag{1}$$

Here $v_{los} = xH(z)L/(1+z) + v_{pec}$ at dimensionless distance x, in box side units, for Hubble parameter $H(z)$ at redshift z and line-of-sight peculiar velocity v_{pec}. The Doppler parameter $b(x) = [2k_B T(x)/m_H]^{1/2}$ for gas at temperature $T(x)$, $\sigma_\alpha = (\pi e^2/m_e c) f_\alpha$ is the total cross-section for Lyα scattering with upward oscillator strength $f_\alpha \simeq 0.4162$, $\lambda_\alpha \simeq 1215.67$ Å is the Lyα wavelength, k_B is the Boltzmann constant and m_H is the mass of a hydrogen atom. As discussed in Appendix A, using a Voigt profile instead negligibly affects the integrated H I absorption profiles we consider. Because of the much higher computational cost of using Voigt profiles, we use only a Doppler profile except where explicitly stated otherwise. For the ENZO simulations, the gridded H I density, temperature and peculiar velocity fields are used. For the GADGET-3 simulations, the spectra are computed along rays using H I-weighted contributions from the particles (Hernquist et al. 1996). To match the resolution of the observations, we smooth the resulting spectra with a Gaussian of full width at half-maximum (FWHM) 8 km s^{-1} for comparison with Rakic et al. (2012) and FWHM 125 km s^{-1} for comparison with Prochaska et al. (2013b).

We extract spectra for a range of impact parameters around haloes identified in the simulations using the grid-based halo finding algorithm described in Paper I. We consider three spectral signatures and their dependence on impact parameter: the 2D absorption as measured by the median Lyα optical depth around the haloes, the Lyα absorption equivalent width and the fractional deviation of the Lyα absorption from the mean intergalactic value. Note the latter two statistics are integrated quantities. The first of these is the equivalent width around a halo at measured velocity v_{halo} along a line of sight to a background QSO, which is computed as

$$w(b_\perp, \Delta v) = \frac{\lambda_\alpha}{c} \int_{v_{halo}-\Delta v/2}^{v_{halo}+\Delta v/2} dv \left[1 - e^{-\tau_\alpha(b_\perp, v)}\right], \tag{2}$$

over a velocity window of width Δv centred on the position of the halo, displaced transversely by an amount $b_\perp$. Following Rakic et al. (2012), we also consider an alternative determination of the equivalent width by dividing the transmission by a factor meant to

correct for the errors incurred in continuum fitting low-resolution spectra. The second integrated absorption statistic we consider is the fractional change δ_F in the flux compared with the mean intergalactic value for the corresponding velocity window, introduced by Prochaska et al. (2013b). It may be expressed in terms of the equivalent widths as

$$\delta_F(b_\perp, \Delta v) = \frac{w(b_\perp, \Delta v) - w_{IGM}}{\Delta \lambda - w_{IGM}}. \tag{3}$$

Here $\Delta \lambda = \lambda_\alpha \Delta v / c$ and $w_{IGM} = \Delta \lambda [1 - \exp(-\tau_{eff})]$, where τ_{eff} is the effective optical depth of the IGM. We adopt the values from Becker et al. (2013) for τ_{eff}. Our simulations recover the mean transmission according to these values to better than 2–4 per cent at $2.0 < z < 2.4$ and to better than 1 per cent at $2.4 < z < 2.8$. Rather than renormalizing the photoionization rates in each simulation to recover the values of τ_{eff} exactly, we take these small deviations to be the uncertainty in the model predictions of the amount of IGM absorption. All the error bars shown for the model predictions are errors in the mean. The error in the mean IGM effective optical depth may be added linearly to the error bars as a systematic uncertainty.

Lastly, in Appendix A we present a series of convergence and parameter tests on these statistical measures. In summary, we find that (a) a box size of 60 Mpc is preferred over 30 Mpc for ENZO simulations to capture statistics on haloes with $M_h > 10^{12} \, M_\odot$; (b) at the resolution of the simulations, radiative transfer effects negligibly affect the predicted integrated H I absorption statistics; (c) when excluding winds, the GADGET-3 results for δ_F are little changed if the quick Lyα method is used to convert gas to stars rather than the algorithm of SH03; (d) for uncertainties σ_H in galaxy systemic velocities and a velocity window Δv, δ_F is insensitive to σ_H for values $\sigma_H < \Delta v / 2$; and (e) for $\sigma_H \approx 500 \, \text{km s}^{-1}$, a velocity window $\Delta v = 2000 \, \text{km s}^{-1}$ provides a good compromise between a sensitive dependence of δ_F on impact parameter and small variance in its values.

3 RESULTS

3.1 An illustrative example of Lyα absorption around a halo

It is instructive to first consider the Lyα absorption around an individual halo in the cosmological simulations. The gas velocity field near a galactic halo is in general complex, involving Hubble flow on large scales, and on smaller, cosmological infall, shocks and streams of merging material. It is important to include a sufficiently large volume around a halo to capture these effects on the simulated spectra. Since the spectra are measured in velocity space, large peculiar motions will furthermore scramble spatial and velocity information. Particularly large displacements in velocity space may result from the cosmological infall around massive haloes.

We illustrate these effects for a $3 \times 10^{12} \, M_\odot$ halo at $z = 2$ from the 30 Mpc GADGET-3 simulation without a wind (G30sfnw), shown in Fig. 1. Three representative lines of sight are shown in the lower panels, one through the halo centre of mass and two offset transversely by ± 1.5 comoving Mpc (cMpc). Despite the high halo gas temperatures, reaching 10^7 K, all three spectra show absorption within $\Delta v \approx \pm 500 \, \text{km s}^{-1}$ of the halo centre of mass. This absorption arises in part as a result of the complex velocity field of the gas. The panel second from the bottom in particular shows the wide range of positions that give rise to line-of-sight velocities matching the systemic velocity of the halo. These lines of sight include the region within the turnaround radius of the gas, $r < r_{t.a.} \simeq 6r_v$, which is sensitive to the star formation and feedback

implementation (Paper I); the virial radius of the halo in Fig. 1 is $r_v = 0.48$ cMpc.

Examining individual absorption features, it is apparent that gas extending out to the turnaround radius contributes to the broad feature at $-50 \, \text{km s}^{-1} < v - v_{h, los} < 150 \, \text{km s}^{-1}$ along the line of sight passing directly through the halo centre. Gas within the turnaround radius also produces the weaker feature at $v - v_{h, los} \simeq 25 \, \text{km s}^{-1}$ along the line of sight displaced laterally by -1.5 Mpc. The line of sight displaced by $+1.5$ Mpc instead probes part of the cosmic web. The very broad absorption feature ranging over $-550 \, \text{km s}^{-1} < v - v_{h, los} < -250 \, \text{km s}^{-1}$ in the spectrum originates in the broad filament attached to the top left of the halo. It is dominated by a system centred at $R_{los} \simeq -5.3$ Mpc, 30 kpc across (proper). It is part of a complex just becoming visible along the left edge of the box in the top panel, along the line of sight. The system has a velocity width of about $160 \, \text{km s}^{-1}$. For comparison, the formal thermal Doppler width ranges over 20–40 km s^{-1} for the gas comprising it. The resulting absorption feature has an equivalent width of 1.2 Å and an H I column density of $N_{H I} = 8 \times 10^{17} \, \text{cm}^{-2}$, forming an LLS along this line of sight (see also Faucher-Giguère & Kereš 2011; Fumagalli et al. 2011; van de Voort et al. 2012; Shen et al. 2013). (Allowing for radiative transfer effects, as discussed in Appendix A, increases $N_{H I}$ to $4 \times 10^{18} \, \text{cm}^{-2}$, but has little effect on the spectrum because the feature is saturated.) The broad spectral feature at $0 < v - v_{h, los} < 150 \, \text{km s}^{-1}$ along the same line of sight originates in a clump centred at $R_{los} \simeq +1.8$ Mpc within the filament extending from the top right of the halo. The complex has a column density of $N_{H I} \simeq 7.4 \times 10^{14} \, \text{cm}^{-2}$ and is velocity broadened by about $100 \, \text{km s}^{-1}$. For comparison, the thermal Doppler width within the structure is $\sim 30 \, \text{km s}^{-1}$. Both these features illustrate the dominating influence of velocity broadening in the vicinity of a massive halo.

The absence of cool gas within the virialized halo, and in particular in the structure at the centre of the halo – the highest density region has a temperature exceeding 10^5 K – suggests the star formation algorithm is inadequate for producing the cool interstellar medium of a galaxy and its nearby surroundings, at least for one within such a massive halo at this redshift. Higher mass resolution, and possibly self-consistent radiative hydrodynamics, likely is required as well. We show below that the models generally produce too little absorption compared with observations within the virial radii of the haloes.

3.2 Median Lyα optical depth

We now turn to consider the observational signature of the neutral hydrogen around galaxy haloes. The most direct measurement of Lyα absorption from the gas around galaxies is the optical depth τ_α. Because of its large variance, the median optical depth is a more stable statistic than the average. Fig. 2 shows the median optical depths, as a function of separation from the halo centres, averaged over simulated spectra in the redshift range $2.0 < z < 2.6$, corresponding to most of the foreground galaxy redshifts in the sample of Rakic et al. (2012). The left-hand panel averages over line-of-sight Hubble flow distances, defined as $r_{los} = v_{los}/H(z)$, within ± 0.4 cMpc of the halo centres. The right-hand panel averages over impact parameters within ± 0.5 cMpc of the halo centres. Both panels show a general rise towards the halo centres, although with differences in the trends. In assigning halo velocities, a random Gaussian error with standard deviation of $\sigma_H = 130 \, \text{km s}^{-1}$ is included to match the data (Rakic et al. 2012).
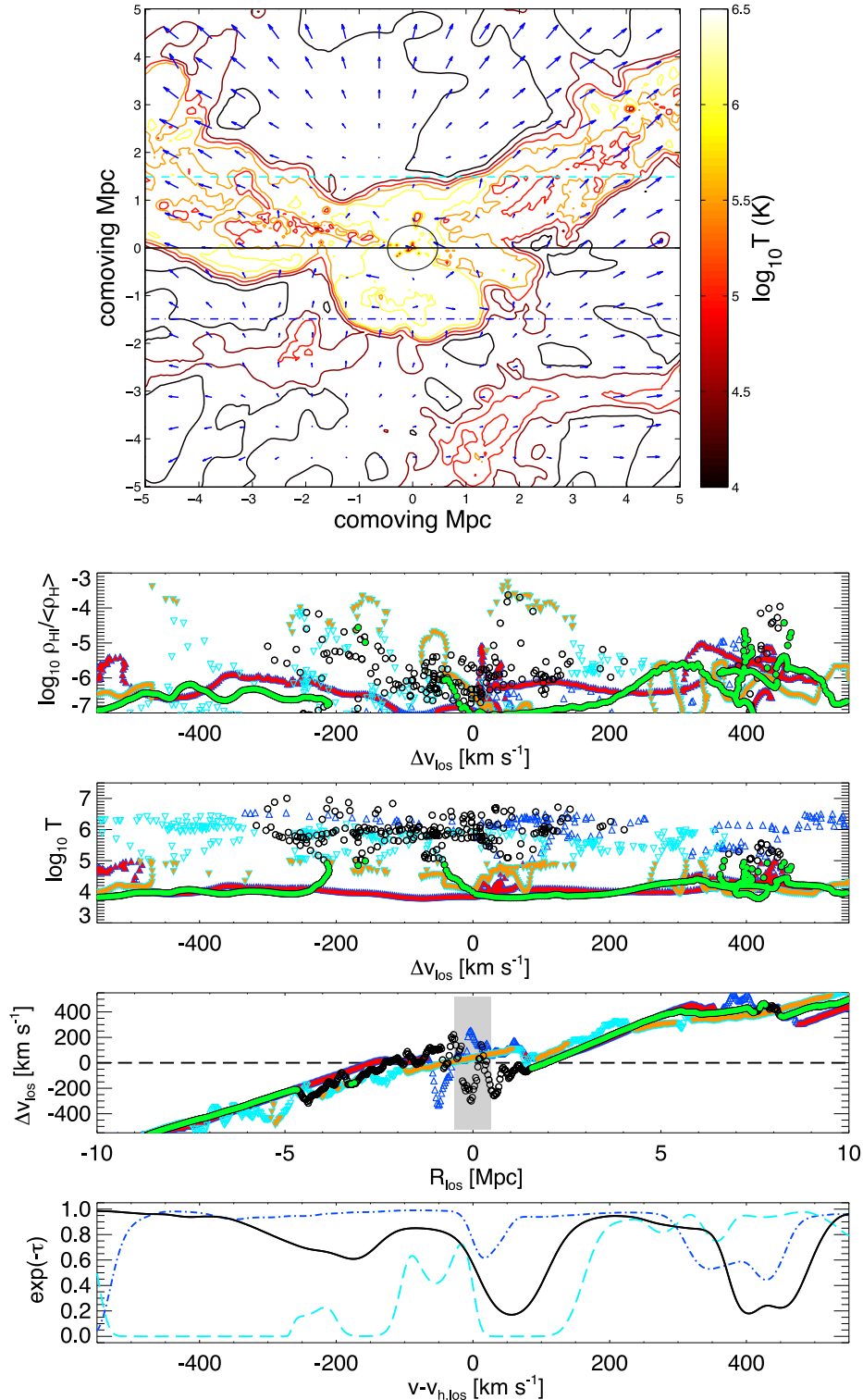
Figure 1. Top panel: H I-weighted temperature and proper velocity fields around a 3×10^{12} M$_\odot$ halo at $z = 2$ from the GADGET-3 30 Mpc box simulation without winds (G30sfnw). The velocities are shown relative to the centre of mass of the halo, where an arrow length equivalent to the spacing of the axis tick marks corresponds to 1000 km s^{-1}. The halo virial radius is represented by a circle. The three Lyα absorption spectra shown in the lower panels are drawn along the lines running parallel to the x-axis. Lower panels: line-of-sight plots showing the H I fraction, $\rho_{\mathrm{H_I}}/\langle\rho_\mathrm{H}\rangle$, and gas temperature T, as functions of the line-of-sight velocity offset Δv_los from the halo centre of mass at $v_{h,\,\mathrm{los}}$. In the second panel from the bottom, Δv_los is shown as a function of the comoving distance, R_los, from the halo centre of mass. The shaded region indicates the size of the virialized zone. Note that regions at multiple values of R_los have $\Delta v_\mathrm{los} \simeq 0$, such that gas outside the hot central region contributes to absorption near and across the systemic velocity of the halo. The bottom panel shows the corresponding spectra. The open black circles, filled green circles and solid black lines are for a line of sight passing through the halo centre of mass. Filled symbols indicate gas with $T < 10^5$ K, and open symbols gas with $T > 10^5$ K. The open cyan and filled orange inverted triangles (open blue and filled red upright triangles) and dashed cyan (dot–dashed blue) lines are for a line of sight laterally offset from the halo centre of mass by $+1.5(-1.5)$ comoving Mpc.
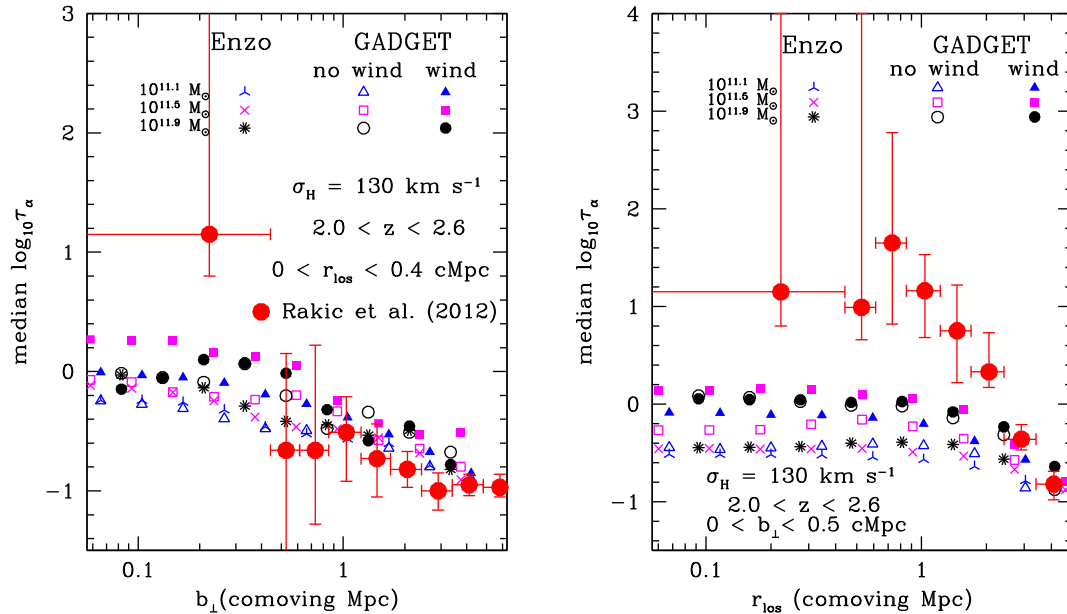
Figure 2. Left-hand panel: median Lyα optical depth, averaged over line-of-sight velocities relative to the halo systemic velocity corresponding to Hubble distances of up to 0.4 Mpc (comoving), against projected separation from the halo. The results are averaged over all haloes in a 0.2-dex-wide mass bin centred at the indicated mass. The model predictions agree with the data except within the typical virial radius, $r_v \simeq 150$–330 kpc (comoving). Right-hand panel: median Lyα optical depth, averaged over projected separations up to 0.5 Mpc (comoving), against line-of-sight Hubble displacement from the halo. Except for the regions along the spectra corresponding to Hubble distances beyond ± 3 Mpc (comoving), the models underpredict the measured absorption. In both panels, halo velocities include a random component drawn from a Gaussian distribution with standard deviation $\sigma_H = 130$ km s^{-1}. The data points (large filled circles; red) are from Rakic et al. (2012). Note that for clarity of presentation, here and for other figures in this paper, the points in each mass bin are grouped with slight offsets using cubic spline interpolation.

For comoving distances outside 0.7 Mpc, all the model predictions in the left-hand panel are in good agreement, with little difference with halo mass. At smaller displacements, the GADGET-3 simulation with star formation (G30sfnw) shows a systematically larger spread in the median optical depths compared with the ENZO simulation (E60_1024). The absorption increases approximately monotonically with halo mass. Generally good agreement is found in comparison with the data of Rakic et al. (2012), except for the innermost point, where the observations show higher absorption than the simulations.

The right-hand panel shows a plateau in the absorption for Hubble flow distances within ± 1 Mpc of the halo centres, and a decline beyond. As in the left-hand panel, the median optical depths in the GADGET-3 simulations exceed those of the ENZO simulation, with the $10^{11.5}$ M$_\odot$ haloes with winds producing the greatest absorption. Outside of 3 Mpc, the median optical depths are in good agreement between all the models, as well as with the measurements of Rakic et al. (2012). The measured values further in, however, greatly exceed all the model predictions.

Similar agreement with the data for the median optical depth as a function of impact parameter was found by Rakic et al. (2013) using the OWLS simulations, with their predictions for the median optical depth along lines of sight passing within the virial radii falling well short of the measured values at Hubble separations from the galaxy smaller than ∼3 Mpc (comoving). They point out that the discrepancy is difficult to assess statistically because the data are highly correlated along the line of sight. The disagreement may also indicate inadequacies in the models, requiring higher mass resolution, full radiative hydrodynamics, an improved star formation model or all three. Agreement improves when averaging over increasingly larger impact parameters. Rather than pursuing further

comparisons with median optical depth measurements, however, we turn next to integrated spectral quantities across wider line-of-sight velocity intervals. We find that these provide a more direct means of discriminating between models.

3.3 The velocity integrated Lyα equivalent width

Rakic et al. (2012) provide absorption equivalent widths within 1000 km s^{-1} wide velocity windows centred on the systemic velocities of the galaxies in their sample. Trainor & Steidel (2012) estimate a median halo mass of $10^{11.9\pm0.1}$ M$_\odot$ for the survey. We consider halo masses within $11 < \log_{10} M_h < 12$. In Fig. 3, the equivalent widths (see equation 2) within a spectral window of width $\Delta v = 1000$ km s^{-1} centred on the halo velocities from the 60 Mpc ENZO simulation (E60_1024) and the GADGET-3 star formation simulations both without (G30sfnw) and with (G30sfw) supernova feedback are shown as a function of impact parameter $b_\perp$, averaged over all haloes in halo mass bins centred at $\log_{10} M_h = 11.1$, 11.5 and 11.9 of width $\Delta \log_{10} M = 0.2$. The simulated spectra have been adjusted by applying a renormalization factor of 0.804 to the fluxes. This matches the renormalization applied by Rakic et al. (2012) to allow for errors in the continuum level in the earlier, lower resolution data of Steidel et al. (2010). The equivalent width values rise towards smaller impact parameters. At $b_\perp > 0.4$ Mpc (comoving), there is little difference between the model predictions. At all impact parameters, the ENZO predictions are nearly independent of halo mass, with the results for the $10^{11.1}$ M$_\odot$ mass bin slightly smaller than the others. By contrast, the GADGET-3 models show a systematic increase with halo mass for $M_h > 10^{11.1}$ M$_\odot$ within the inner 0.4 Mpc. For reference, the virial radius ranges over 150–330 kpc for
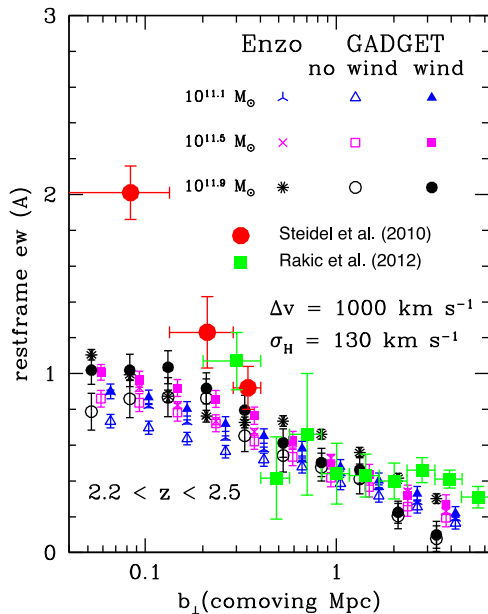
Figure 3. Rest-frame equivalent width (Å) within a velocity window $\Delta v = 1000 \, \mathrm{km \, s^{-1}}$ centred on the halo centre-of-mass velocity as a function of line-of-sight impact parameter $b_\perp$ for halo masses $\log_{10} M_{\mathrm{h}} = 11.1$ (triangles; blue), 11.5 (squares; magenta) and 11.9 (circles; black) at redshifts $2.2 < z < 2.5$. The data are from Steidel et al. (2010, large solid circles; red) and Rakic et al. (2012, large filled squares; green).

10^{11}–$10^{12} \, \mathrm{M_\odot}$ haloes.[1] The models including supernova feedback predict somewhat larger equivalent widths compared with the same mass halo with star formation alone. This produces a degeneracy in the predictions: a given equivalent width value may be produced either by a halo with star formation and no wind or a lower mass halo with star formation and a wind.

Comparison with the equivalent width measurements of Steidel et al. (2010, large red filled circles) and Rakic et al. (2012, large green filled squares) shows that the model predictions agree well with the data outside the virial radius. At $b_\perp > 3 \, \mathrm{Mpc}$ (comoving), the models underpredict the measured values somewhat. Assessing the statistical significance of the difference is not straightforward since the lines of sight in a given simulation are correlated, as they are drawn from the same haloes. There may also be a slight residual offset in the continuum renormalization applied by Rakic et al. (2012). In the range of agreement, the differences between the feedback and non-feedback models are too small for the data to discriminate between them.

3.4 Deviation of Lyα absorption from the mean IGM

The absorption excess δ_{F} relative to the mean IGM, as quantified by the effective optical depth τ_{eff}, averaged over a spectral window $\Delta v = 1000 \, \mathrm{km \, s^{-1}}$ at $z = 2.2$, is shown in Fig. 4. Results are displayed for the ENZO 60 Mpc box (E60_1024) and the GADGET-3 simulation with star formation but no winds (G30sfnw), averaged over all haloes in mass bins centred at $\log_{10} M_{\mathrm{h}} = 11.1$, 11.5 and 11.9 of width $\Delta \log_{10} M = 0.2$. At projected separations $b_\perp > 300 \, \mathrm{kpc}$ (co-

moving), all the models agree, showing a rise towards the halo centres (left-hand panel). The non-zero values rising towards the halo centres demonstrate excess absorption above the average IGM value in an extended region outside the haloes, well outside the turnaround radii of the haloes ($r_{\mathrm{t.a.}} \sim 1.8 \, \mathrm{cMpc}$ for $M_{\mathrm{h}} = 10^{11.9} \, \mathrm{M_\odot}$). While the results for the ENZO simulation show essentially no variation with halo mass, the absorption systematically rises within the virial radius with halo mass in the GADGET-3 simulations for haloes more massive than $10^{11.1} \, \mathrm{M_\odot}$. At projected separations smaller than the virial radius, the absorption in the GADGET-3 simulation lies below the ENZO values for halo masses below $10^{11.6} \, \mathrm{M_\odot}$. We note that star formation in the GADGET-3 simulation substantially reduces the gas density within the virial radius compared with the gas-conserving ENZO simulations (Paper I).

The excesses increase slowly with redshift, as shown in the right-hand panel of Fig. 4, rising by only about 50 per cent from $z = 2$ to 3. The trend of increasing absorption with halo mass near the halo centres weakens for the GADGET-3 models with increasing redshift, except that the absorption for the $10^{11.9} \, \mathrm{M_\odot}$ mass bin tends to stay the largest. The different models also continue to show the same level of absorption at large distances, here shown by the $10^{11.5} \, \mathrm{M_\odot}$ haloes at $b_\perp = 1.5 \, \mathrm{Mpc}$.

Thus far we have compared the simulations with Lyα absorption data around SFGs. In the left-hand panel of Fig. 5, we instead compare with the δ_{F} measurements surrounding QSOs reported by Prochaska et al. (2013b) at $z \approx 2.4$, with a velocity window $\Delta v = 2000 \, \mathrm{km \, s^{-1}}$. A random component drawn from a Gaussian distribution with $\sigma_{\mathrm{H}} = 520 \, \mathrm{km \, s^{-1}}$ is added to the halo velocities to match the typical errors in the measured halo redshifts. The predictions for the $M_{\mathrm{h}} > 10^{12} \, \mathrm{M_\odot}$ haloes in the ENZO simulation lie lower than those for the GADGET-3 simulations within the turnaround radius, $r_{\mathrm{t.a.}} \sim 1.8 \, \mathrm{Mpc}$, although the smaller box for the GADGET-3 simulations results in larger uncertainties because they contain only about a dozen haloes in this mass range. The measurements outside the virial radius agree with all the models. The innermost point, however, is consistent only with the $M_{\mathrm{h}} > 10^{12} \, \mathrm{M_\odot}$ halo predictions from the GADGET-3 simulations, although this may again only be a consequence of the large error bars.

The fluctuations in the mean transmitted flux, given by $\sigma_{\mathrm{F}} = \langle (F - \langle F \rangle)^2 \rangle^{1/2}$, are shown in the right-hand panel of Fig. 5 at $z = 2.4$. The ratio $\sigma_{\mathrm{F}}/\langle F \rangle$ is nearly constant at 0.10–0.15 with $b_\perp$ for all the models. This is substantially smaller than the measured fluctuations, especially within the turnaround radius. Although the reported values include continuum errors, so that they may perhaps be conservatively taken as upper limits, the discrepancy may indicate the need for additional astrophysical effects which increase the variance in transmitted flux between lines of sight, such as QSO beaming or a fluctuating magnetic field (Pandey & Sethi 2013; Chongchitnan & Meiksin 2014).

Finally, a further independent test of the models is provided by estimating the covering fractions f_{C} for high equivalent width absorption. We define an excess integrated equivalent width relative to the mean IGM as

$$\Delta w_0 (b_\perp, \Delta v) = \frac{\lambda_\alpha}{c} \int_{v_{\mathrm{halo}} - \Delta v/2}^{v_{\mathrm{halo}} + \Delta v/2} \mathrm{d} v \left[\mathrm{e}^{-\tau_{\mathrm{eff}}} - \mathrm{e}^{-\tau_\alpha (b_\perp, v)} \right], \quad (4)$$

where τ_{eff} is the IGM effective optical depth. We remove the contribution from the intervening large-scale IGM because it is non-negligible and we wish to focus on the fluctuations arising from the galaxy environment (see Section 4.2). The covering fraction is then the ratio of the number of lines of sight with Δw_0 above a given threshold to the total number of lines of sight.

---

[1] The comoving virial radius is $r_{\mathrm{v}} \simeq 0.33 M_{\mathrm{h,12}}^{1/3}$ Mpc for a halo mass $10^{12} M_{\mathrm{h,12}} \, \mathrm{M_\odot}$. The turnaround radius, where the infall peculiar velocity cancels the Hubble flow, is at $r_{\mathrm{t.a.}} \simeq 6 r_{\mathrm{v}}$ (Paper I).
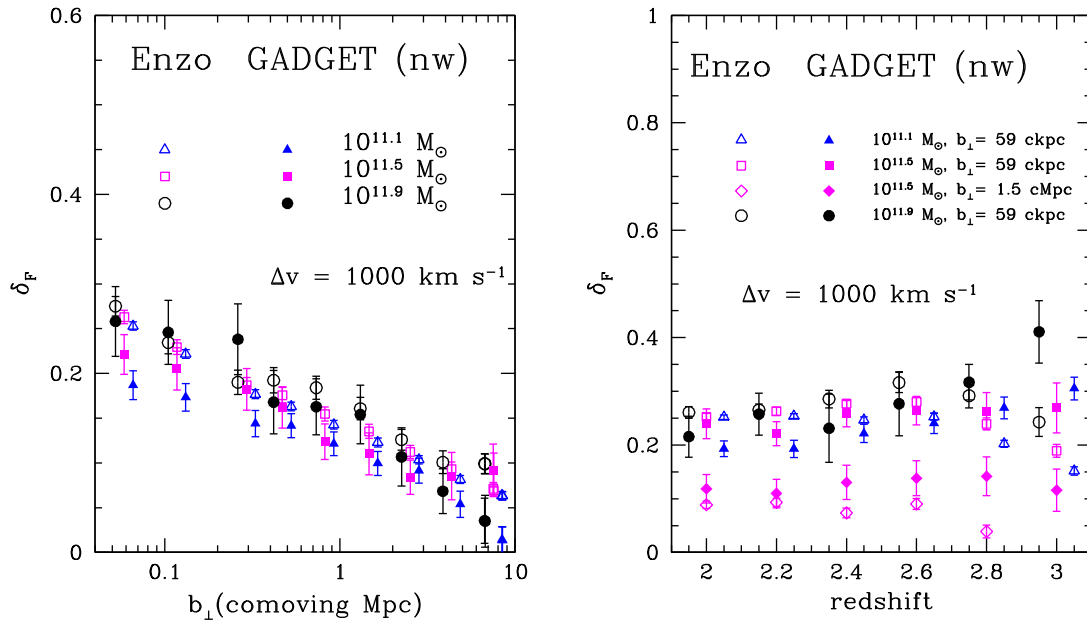
Figure 4. Fractional absorption excess δ_F relative to the mean IGM absorption, for a spectral window $\Delta v = 1000 \, \text{km s}^{-1}$ wide across the halo systemic redshifts for the ENZO 60 Mpc box simulation (E60_1024) and the GADGET-3 simulation with star formation but no wind (G30sfnw). Left-hand panel: the variation of δ_F with projected impact parameter $b_\perp$ and halo mass at $z = 2.2$. Absorption exceeds the average IGM contribution out to several comoving Mpc. Right-hand panel: the evolution of δ_F with redshift for selected values of $b_\perp$ and halo mass. The symbols are as indicated on the diagram. In both panels, halo velocities include a random component drawn from a Gaussian distribution with standard deviation $\sigma_H = 130 \, \text{km s}^{-1}$.
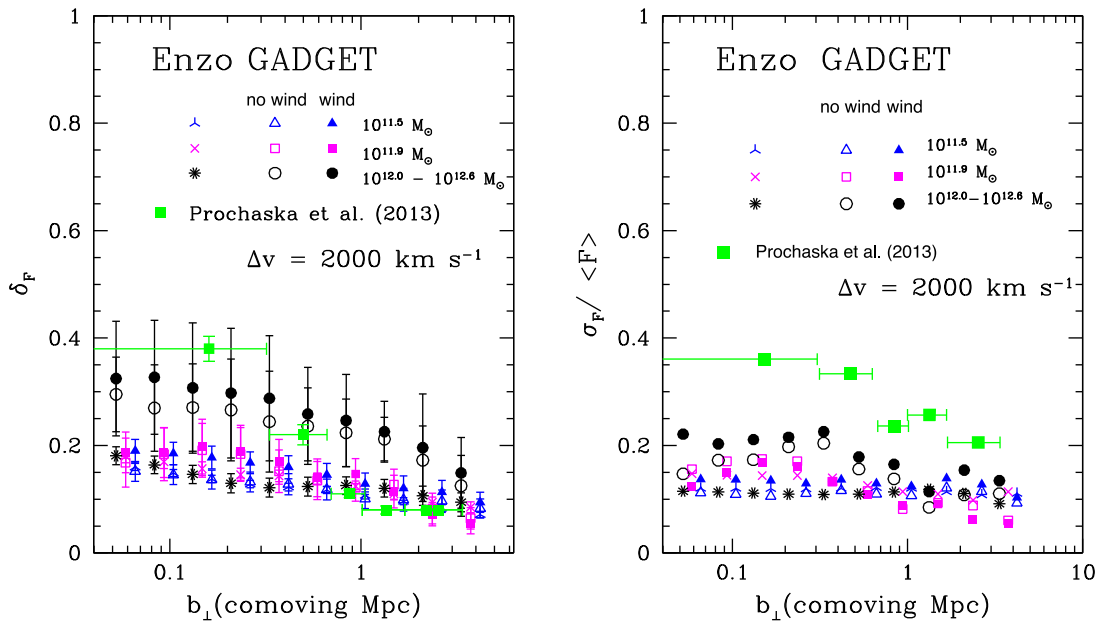

Figure 5. Left-hand panel: fractional absorption excess δ_F relative to the mean IGM absorption, for a spectral window $\Delta v = 2000 \, \text{km s}^{-1}$ across the halo systemic velocities for the ENZO 60 Mpc box simulation (E60_1024) and the GADGET-3 simulations with (G30sfw) and without (G30sfnw) a wind. The data points in the left-hand panel are for absorption around QSOs taken from Prochaska et al. (2013b), with the error bars showing the errors in the mean. Right-hand panel: the fluctuations relative to the mean transmitted flux, $\sigma_F/\langle F \rangle$ (see the text for details). Both δ_F and $\sigma_F/\langle F \rangle$ are shown against projected impact parameter $b_\perp$ at $z = 2.4$. The halo velocities include a random component drawn from a Gaussian distribution with standard deviation $\sigma_H = 520 \, \text{km s}^{-1}$.

The results for $\Delta w_0 > 1.0 \, \text{Å}$ are shown in Fig. 6 for the ENZO 60 Mpc box (E60_1024) and the GADGET-3 simulations with (G30sfw) and without (G30sfnw) winds. The left-hand panel is for absorption in the velocity window $\Delta v = 1000 \, \text{km s}^{-1}$ at $2.0 < z < 2.6$ and the right for $\Delta v = 2000 \, \text{km s}^{-1}$ at $z = 2.4$. The covering fractions rise towards the halo centres in all the mod-

els. Within the virial radius, the GADGET-3 models show an increase with halo mass and generally systematically higher values for the models including wind feedback, especially for the narrower velocity window in the left-hand panel. The more massive haloes with winds achieve covering fractions $f_C > 0.5$ well within their virial radii.
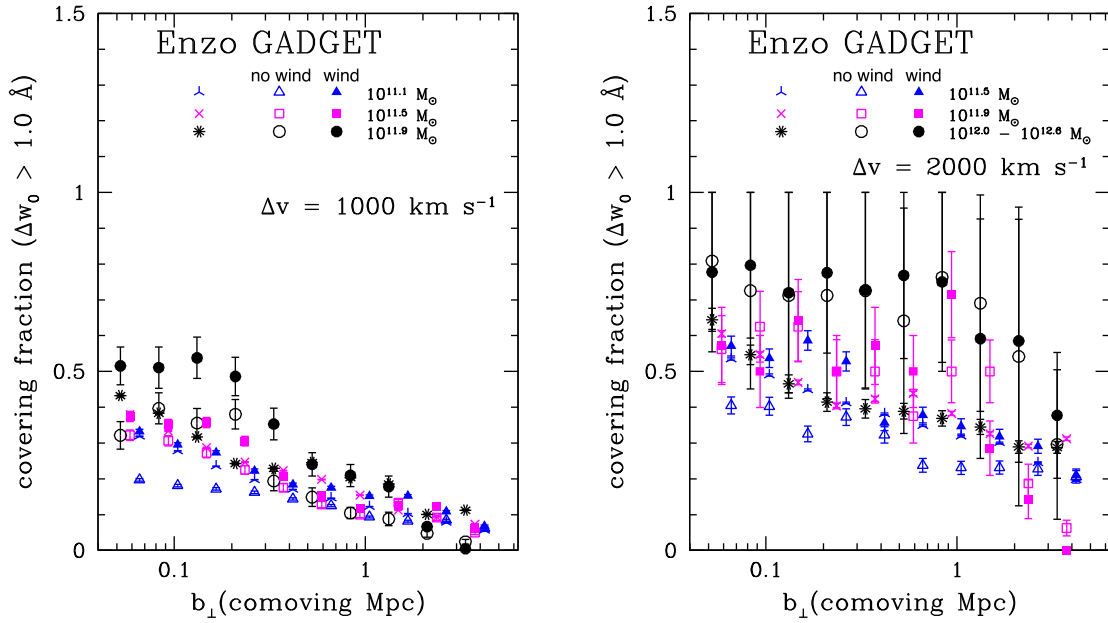
Figure 6. Covering fraction f_C for excess rest-frame equivalent widths of $\Delta w_0 > 1.0$ Å above the mean intergalactic value over spectral windows of width $\Delta v = 1000 \, \text{km} \, \text{s}^{-1}$ (left-hand panel) and $\Delta v = 2000 \, \text{km} \, \text{s}^{-1}$ (right-hand panel) across the halo systemic velocities for the ENZO 60 Mpc box (E60_1024) and the GADGET-3 simulations with (G30sfw) and without (G30sfnw) a wind. The covering fraction is shown against projected impact parameter $b_\perp$ at $2.0 < z < 2.6$ in the left-hand panel and at $z = 2.4$ in the right-hand panel. The rise towards small impact parameters increases with increasing halo mass for the GADGET-3 simulations. Within the virialized region, the models with a wind generally lie systematically above those without. The halo velocities include a random component drawn from a Gaussian distribution with standard deviation $\sigma_H = 130 \, \text{km} \, \text{s}^{-1}$ (left-hand panel) or $\sigma_H = 520 \, \text{km} \, \text{s}^{-1}$ (right-hand panel).
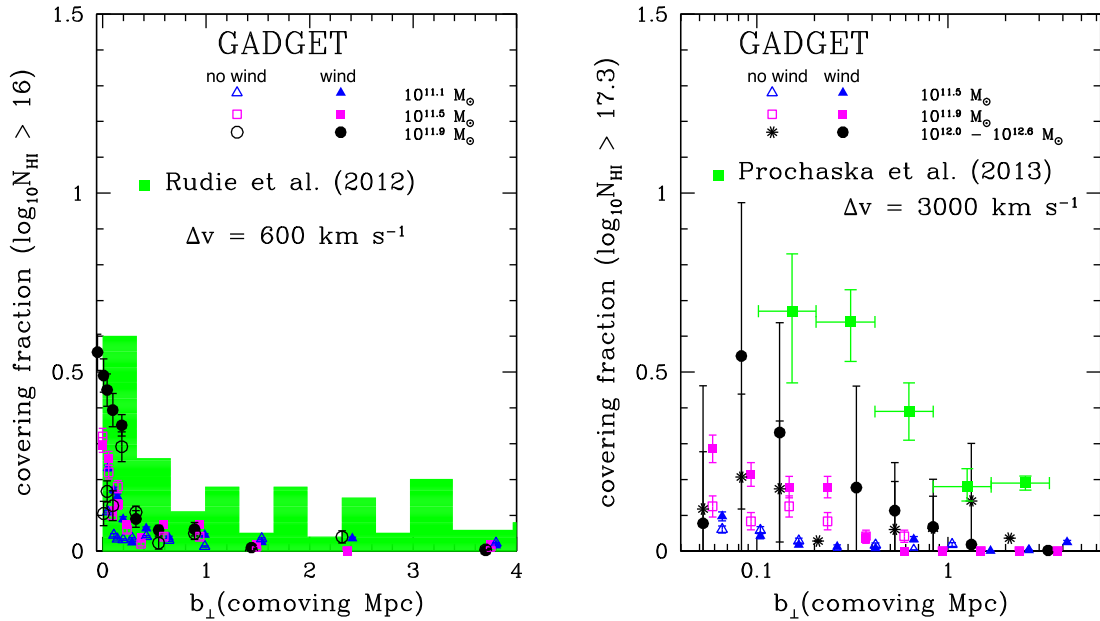
Figure 7. Covering fraction f_C for discrete absorption systems with column densities $N_{\text{H I}} > 10^{16} \, \text{cm}^{-2}$ within a spectral window of width $\Delta v = 600 \, \text{km} \, \text{s}^{-1}$ across the halo systemic velocities (left-hand panel) and $N_{\text{H I}} > 10^{17.3} \, \text{cm}^{-2}$ for a window $\Delta v = 3000 \, \text{km} \, \text{s}^{-1}$ (right-hand panel) for the GADGET-3 simulations with (G30sfw) and without (G30sfnw) a wind. The covering fraction is shown against projected impact parameter $b_\perp$ at $z = 2.3$. The halo velocities include a random component drawn from a Gaussian distribution with standard deviation $\sigma_H = 130 \, \text{km} \, \text{s}^{-1}$ (left-hand panel) or $\sigma_H = 520 \, \text{km} \, \text{s}^{-1}$ (right-hand panel).

While the integrated excess equivalent widths are straightforward to measure from observations, the focus of recent literature has been the covering fractions of identified discrete absorption systems. A direct comparison with the simulations would require absorption line identification and fitting, which we defer to later work. Here, we use the higher spatial resolution of the GADGET-3

simulations to provide illustrative comparisons by identifying discrete contiguous H I systems along the lines of sight directly from the physical gas data. We include a correction for radiative transfer following Rahmati et al. (2013), as described in Appendix A. In Fig. 7, we compare the predicted covering fractions with the observations of Rudie et al. (2012) for systems with H I column densities

$N_{\rm H\,I} > 10^{16}\,{\rm cm^{-2}}$ within a velocity window $\Delta v = 600\,{\rm km\,s^{-1}}$ wide centred on the galaxy systemic velocities (left-hand panel), and with the data of Prochaska et al. (2013b) for 'optically thick' absorbers in a velocity window $\Delta v = 3000\,{\rm km\,s^{-1}}$ wide centred on the galaxies (right-hand panel). These authors define optically thick absorbers variously as those showing obvious damping wings, Lyman limit absorption, strong low-ionization metal absorption or (if not classifiable otherwise) exhibiting a single strong Lyα feature with $w_0 > 1.8\,{\rm \AA}$. We select discrete systems from the simulations with column densities $N_{\rm H\,I} > 10^{17.3}\,{\rm cm^{-2}}$. We note that the velocity window is so wide that the statistics of the discrete systems are not fully independent, introducing additional modelling uncertainties; since most of the absorption arises near the galaxy, however, this is expected to be a small effect.

The covering fraction of systems with $N_{\rm H\,I} > 10^{16}\,{\rm cm^{-2}}$ is small compared with the measurements for most of the models, particularly within the virial radius. The exception is for massive haloes, $M_{\rm h} > 10^{11.8}\,{\rm M_\odot}$, for which the model with a wind shows a rapid rise in the covering fraction towards the halo centre close to the measured values. The covering fractions for absorbers optically thick at the Lyman limit ($N_{\rm H\,I} > 10^{17.3}\,{\rm cm^{-2}}$) lie systematically below the observations of Prochaska et al. (2013b) by a factor of 4 within the turnaround radius of haloes ($b_\perp \lesssim 2$ Mpc); at larger radii they are essentially absent in the simulations. While the covering fraction for $M_{\rm h} > 10^{12}\,{\rm M_\odot}$ approaches the measured values within the spread from the simulation, the uncertainties in the mean are large due to the small number of haloes available in this mass bin (a total of 12). This, along with the heterogeneous definition of the observed optically thick absorbers, makes it difficult to quantify statistically the level of disagreement. Moreover, Prochaska et al. (2013b) caution against errors due to continuum placement and line-blending. Similarly, low covering fractions compared with observations are found Fumagalli et al. (2014) and Faucher-Giguere et al. (2015) for halo masses exceeding $10^{12}\,{\rm M_\odot}$. By contrast, a recent study by Rahmati et al. (2015) finds close agreement with the measured values, which they attribute to their feedback model. Their comparison, however, is for larger mass haloes, $M_{\rm h} > 10^{12.5}\,{\rm M_\odot}$, captured within their larger simulation volume. It should also be noted that the simulations other than ours compute the covering fractions based on integrated line-of-sight column densities rather than discrete absorption systems.

4 DISCUSSION

4.1 Radial characteristics of the absorption

We have compared the statistics for Lyα absorption along lines of sight passing through the environments of galaxy haloes using three simulations: an ENZO simulation without star formation and two GADGET-3 simulations with star formation, one of which also allows for feedback in the form of supernova-driven winds. We found in Paper I that the gas properties of the haloes largely agree beyond the turnaround radius, regardless of the inclusion of star formation or winds. The results presented here confirm that the predicted absorption line statistics for lines of sight passing outside the turnaround radius are similar.

Comparisons with the Lyα absorption statistics in SFGs (Steidel et al. 2010; Rakic et al. 2012) and QSOs (Prochaska et al. 2013b) demonstrate that the simulations successfully recover the absorption statistics outside the halo virialized regions over a decade in length-scales, to a varying level of accuracy. Within the virial ra-

dius, however, the measured amount of integrated absorption rises to a level none of the models reproduce. A similar trend is found using the median Lyα optical depth data for SFGs (Fig. 2).

The various absorption line statistics nevertheless show some common trends among the models. The predictions of all the models, whether or not they include star formation or wind feedback, all agree, within the error bars, outside the turnaround radii of the haloes. The models also agree well with the data for both SFGs and QSOs in this region. As the virial radius is approached, however, the models begin to diverge.

The gas around galaxies has generally been divided between a CGM within a distance of $\sim$300 kpc (proper) from a galaxy (e.g. Steidel et al. 2010; Prochaska et al. 2013b) and the IGM on larger scales. Based on our simulation results, we rather suggest that it is useful to consider three distinct regions: the inner virialized region, an intermediate region we call the 'mesogalactic medium' (MGM), extending between the virial radius and the IGM ($r_{\rm v} < r < 12r_{\rm v}$), and the IGM well outside galactic haloes ($r > 12r_{\rm v}$). The virialized region is distinguished as the active theatre within which star formation and feedback most affect the hydrogen absorption signatures. Here, discrete optically thick absorption systems, especially DLAs, for which radiative transfer effects will be particularly important, may make substantial contributions to the integrated amount of absorption. The MGM is the region around galaxies exhibiting enhanced absorption over the diffuse IGM, but little affected by star formation or feedback. It originates from gas in the extended haloes around galaxies (Paper I), before merging into the diffuse IGM on larger scales.

4.2 From where does the measured absorption arise?

Many of the H I absorption observational studies around galaxies have focused on the search for evidence of the cold streams predicted to penetrate into the virialized regions of moderate-mass galactic haloes ($M_{\rm h} < 10^{12}\,{\rm M_\odot}$). Establishing that the absorption arises from inward streaming gas is observationally challenging; indeed, the measured kinematics favour outflows (Steidel et al. 2010). The measured covering fractions of cold ($T \approx 10^4$ K) gas appear to exceed theoretical expectations in both SFGs (Rakic et al. 2012) and QSOs (Prochaska et al. 2013b). The excess absorption in QSOs is especially intriguing, as the gas interior to the virial radius is expected to be shock heated to such high temperatures as to be in collisional ionization equilibrium, with greatly reduced levels of neutral hydrogen. As shown in Fig. 1, the absorption signal as a function of impact parameter is complicated by the complex peculiar velocity field of the gas. The large peculiar motions of the gas in the vicinity of galaxies can shift the absorption contribution of gas parcels distant from the galaxies into and out of the velocity window used to measure the absorption signature.

In order to gain some insight into the origin of the measured absorption signatures, we construct spectra from the ENZO 60 Mpc simulation after masking all the H I within the virial radius of haloes more massive than $M_{\rm h} > 10^{11}\,{\rm M_\odot}$. The resulting effect on the integrated equivalent width in a velocity window $\Delta v = 1000\,{\rm km\,s^{-1}}$ wide centred on the galaxy velocities is shown in the left-hand panel of Fig. 8 (open symbols). While the contribution of gas external to the virialized region to the absorption signature decreases towards small impact parameters for $b_\perp < r_{\rm v}$, it never vanishes. At least 70 per cent of the integrated absorption at $b_\perp \ll r_{\rm v}$ arises from gas outside the virialized zone.

In terms of the absolute equivalent width values, Fig. 3 shows that within the virial radius the simulations underpredict the
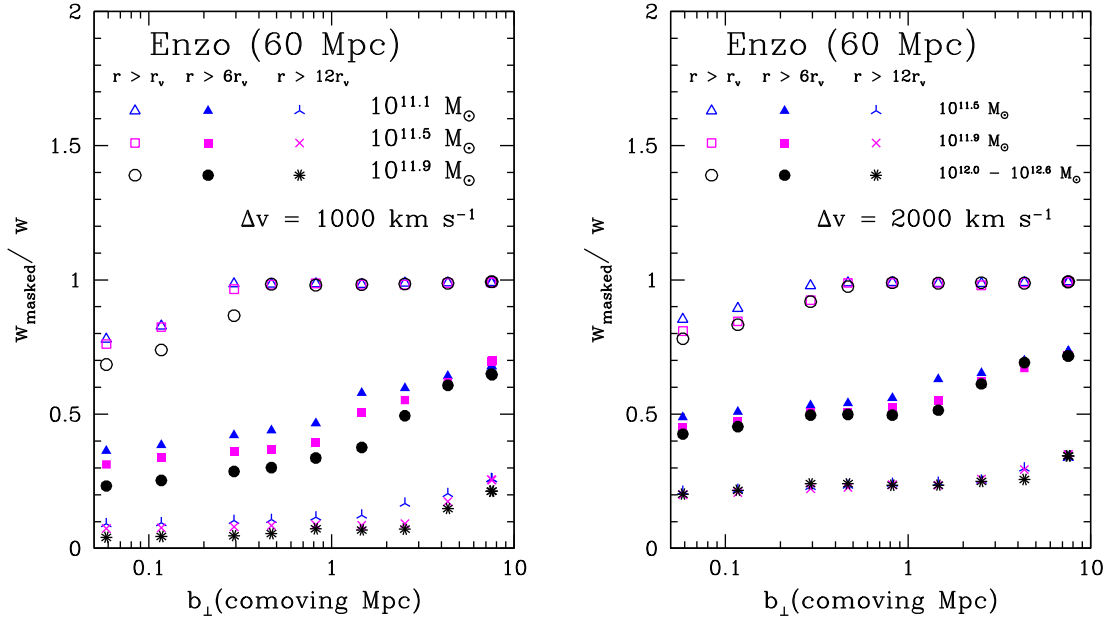
Figure 8. Fraction of equivalent width arising from gas outside the virialized region, $r > r_v$ (open symbols), outside the turnaround radius, $r > 6r_v$ (solid symbols), and outside the mesogalactic region, $r > 12r_v$ (starred symbols), shown against projected comoving impact parameter $b_\perp$ at $z = 2.4$. The equivalent widths are computed within spectral windows of width $\Delta v = 1000\,\mathrm{km\,s^{-1}}$ (left-hand panel) or $2000\,\mathrm{km\,s^{-1}}$ (right-hand panel) across the halo systemic velocities for the ENZO 60 Mpc box (E60_1024). In both panels, most of the absorption for lines of sight passing within the virial radius arises from gas outside the virialized region, and about a third from gas outside the turnaround radius. The halo velocities include a random component drawn from a Gaussian distribution with standard deviation $\sigma_H = 130\,\mathrm{km\,s^{-1}}$ (left-hand panel) or $520\,\mathrm{km\,s^{-1}}$ (right-hand panel).

measured equivalent width by $\Delta w_0 \simeq 1\,\mathrm{\AA}$ compared with observations. About half the mean absorption is thus missing within the virial radius. Zoom-in simulations, achieving a baryon mass resolution of about $10^5\,\mathrm{M_\odot}$ for haloes more massive than $10^{11}\,\mathrm{M_\odot}$, find covering fractions for saturated absorption lines smaller than 50 per cent (e.g. Fumagalli et al. 2011, 2014; Goerdt et al. 2012). Until damping wings appear ($N_{\mathrm{H\,I}} > 10^{19}\,\mathrm{cm^{-2}}$), an individual saturated line will contribute only about $\Delta w_0 \simeq 0.5\,\mathrm{\AA}$. Given the covering fraction, this is too small to make up the difference. Systems with column densities $N_{\mathrm{H\,I}} > 10^{19}\,\mathrm{cm^{-2}}$, or equivalent widths of 2–$3\,\mathrm{\AA}$, are rare, with covering fractions well under 10 per cent in these simulations, so that including systems showing damping wings cannot fully make up the difference either. The simulations of Faucher-Giguere et al. (2015), with a baryon resolution as small as $4 \times 10^4\,\mathrm{M_\odot}$, however, show a higher incidence rate of damped absorbers. For haloes more massive than $10^{11}\,\mathrm{M_\odot}$, the covering fractions for saturated lines reach 60–80 per cent within the virial region and 20–40 per cent for systems with $N_{\mathrm{H\,I}} > 10^{19}\,\mathrm{cm^{-2}}$. This may just be sufficient to make up the missing absorption from the virialized zone. If systems with damped wings account for the missing absorption and their covering fractions are moderate or small, then wide variations in the integrated absorption between different lines of sight would result, with the absorption found in the simulations presented here providing a more constant baseline level.

Masking out the region within the turnaround radius ($r < 6r_v$) further reduces the signal, but the contribution to absorption within $b_\perp < 6r_v$ from material outside the turnaround radius is still non-negligible. Gas at $r > 6r_v$ contributes at least 25 per cent of the absorption signal we obtain even at $b_\perp \ll r_v$ (by comparison, less than 10 per cent of the signal derives from the diffuse IGM, at $r > 12r_v$). At transverse separations outside the turnaround radius, the full absorption signal is still not achieved, demonstrating that

about 20 per cent of the absorption along a line of sight passing through the mesogalactic region of a given halo arises from mesogalactic gas in other haloes. For a halo of mass $M_\mathrm{h} = 10^{11.9}\,\mathrm{M_\odot}$, this corresponds to absorption from material at a distance beyond 1.8 Mpc (comoving), or a velocity offset of $130\,\mathrm{km\,s^{-1}}$, well within the velocity window $\Delta v = 1000\,\mathrm{km\,s^{-1}}$.

Increasing the velocity window to $\Delta v = 2000\,\mathrm{km\,s^{-1}}$ (Fig. 8, right-hand panel) produces similar trends. Results for halo masses corresponding to the host galaxies of QSOs ($12.0 < \log_{10} M_\mathrm{h} < 12.6$) are now also shown. For the increased velocity window, even for these massive haloes 80 per cent of the integrated absorption signal at small transverse impact parameters ($b_\perp \ll r_v$) originates in gas outside the virialized region. About half the signal for lines of sight passing within the turnaround radius originates from gas beyond the turnaround radius, while 20 per cent of the absorption for lines of sight passing through the virialized and mesogalactic regions originates from gas in the diffuse IGM.

5 CONCLUSIONS

We perform large-scale cosmological hydrodynamical simulations using two numerical schemes, GADGET-3, including star formation using the prescription of SH03, with and without supernova-driven wind feedback, and ENZO without star formation as a control case. The simulations allow us to assess the impact of star formation and wind feedback separately on the H I absorption statistics around galaxies and QSOs. The statistical measures we consider are based primarily on the integrated absorption properties within velocity windows centred on the systemic velocities of the galactic haloes: equivalent width values, fractional absorption excesses relative to the mean IGM and fluctuations in the absorbed flux. We also provide statistical predictions for covering fractions of integrated equivalent

width values over the velocity windows and for some discrete absorption systems. We investigate the possible effects of radiative transfer on the statistics considered. We find that radiative transfer corrections do not affect much the statistics for absorption signatures integrated over broad velocity windows. This is because the corrections are small for optically thin systems, while they affect little the equivalent widths of saturated features. The exception would be for damped or near damped Lyα systems, for which radiative transfer corrections could substantially increase the equivalent widths. Because the corrections do not allow for the hydrodynamical response of the gas to the much reduced photoelectric heating rates, an accurate assessment of the contribution from damped systems requires a self-consistent radiative hydrodynamics treatment. We therefore restrict our discussion of discrete absorption systems to those that would still be highly ionized. We include a correction for radiative transfer for these systems. We compare the simulation results with the measurements of Steidel et al. (2010), Rakic et al. (2012) and Rudie et al. (2012) for SFGs and Prochaska et al. (2013b) for QSOs over the redshift range $2 < z < 3$.

On the basis of the simulated absorption properties, we identify three regions in the gas surrounding a galaxy with distinct absorption properties, the inner virialized region, a mesogalactic zone extending from the virial radius to twice the turnaround radius ($r_{\mathrm{t.a.}} \simeq 6r_{\mathrm{v}} \approx$ 1–3 cMpc for $10^{11.0}$–$10^{12.6}$ M$_\odot$ haloes) and the IGM beyond. The simulations show that star formation and wind feedback play only a secondary role in establishing the integrated H I absorption signatures compared with the general trend of increasing absorption for decreasing impact parameter. All the simulations reproduce the integrated absorption measurements within the MGM and beyond. This is a non-trivial result since it extends the success of IGM simulations in the context of a ΛCDM cosmology, from the diffuse IGM to the extended haloes of galaxies down to their virial radii, without being subject to the uncertainties of subgrid physics. As such, the agreement is a confirmation of the ΛCDM cosmological model for structure formation on comoving scales down to $\sim$0.4 Mpc around galaxies over the redshift range $2 < z < 3$.

The GADGET-3 simulations, both with and without a wind, and the ENZO 60 Mpc box simulation produce comparable equivalent width values in $\Delta v = 1000 \, \mathrm{km \, s^{-1}}$ windows centred on the halo systemic velocities over the full range of impact parameters. Allowing for a wind, all the model predictions for haloes with masses $M_{\mathrm{h}} > 10^{11.4}$ M$_\odot$ agree with the measurements of Steidel et al. (2010) and Rakic et al. (2012) outside the virial radius, over projected separations in the range $0.5 \lesssim b_\perp \lesssim 2$ Mpc (comoving). The agreement between the GADGET-3 and ENZO simulations on both the gas properties, as shown in Paper I, and the absorption properties examined here, suggests that the simulations adequately resolve the structures that dominate the integrated absorption signatures in this region. Within the virialized region, the GADGET-3 models show a secondary trend of increasing absorption with halo mass and enhanced absorption for a given halo mass when wind feedback is included, producing a degeneracy between halo mass and wind feedback, at least for the feedback model we adopt. All the models, however, underpredict the amount of absorption compared with observations for lines of sight passing through the virialized regions. High-resolution zoom-in simulations including radiative transfer suggest that LLSs, especially DLAs, may account for the remaining absorption. The discrepancy may also indicate the need for a more sophisticated star formation and feedback model.

We also compare our models with the median optical depth measurements of Rakic et al. (2012). The models agree well with the measurements outside the virial radius, where all the models show

similar values, but not within, similar to the integrated equivalent width comparisons. In addition to possibly being a consequence of unresolved absorption systems, the shortfall may also be in part statistical, a consequence of line-of-sight correlations in the median optical depth values on small scales (we refer the reader to Rakic et al. 2013, for a discussion).

We also compare the model predictions for the fractional absorption excess δ_{F} with the data of Prochaska et al. (2013b), who report measured values in velocity windows $\Delta v = 2000 \, \mathrm{km \, s^{-1}}$ centred on QSOs. In the mesogalactic region, both the ENZO and GADGET-3 simulation predictions are largely insensitive to the halo mass. Agreement with the measured values is achieved even for halo masses below $M_{\mathrm{h}} > 10^{12.0}$ M$_\odot$, the expected lower halo mass of QSO host galaxies. The ENZO simulation underpredicts the amount of absorption within the virial radius, as found for SFGs. The comparison with the GADGET-3 simulations is inconclusive because of the low number of massive haloes in the simulation volume.

We compute covering fractions for integrated equivalent widths within the velocity windows, as these are readily measured from observations without the requirement of identifying and fitting discrete absorption systems in the spectra. The sensitivity we find to feedback suggests that the covering fractions may provide useful constraints on feedback models. Since much of the literature focuses instead on the covering fraction of discrete absorption systems, we also consider illustrative comparisons with observations for saturated absorption lines. We find good agreement with observations of SFGs, but underpredict the covering fraction of optically thick absorbers in QSOs, with only marginal agreement with the observations. Because of the low number of massive haloes in our simulations, however, the statistics are too poor to be conclusive. Agreement may require larger mass haloes than may be examined with the limited box size analysed here. An accurate determination of the contributions from individual LLSs and DLAs to the absorption properties within the virialized region may also require the increased resolution of zoom-in simulations. Recovering the full amount of absorption from virialized gas will likely require additional physical effects, including alternative subgrid feedback models, self-consistent radiative hydrodynamics to account for the physical response of systems optically thick to ionizing radiation or possibly pressure resulting from a fluctuating magnetic field.

REFERENCES

Abazajian K. N. et al., 2009, ApJS, 182, 543

Ahn C. P. et al., 2012, ApJS, 203, 21

Becker G. D., Bolton J. S., Haehnelt M. G., Sargent W. L. W., 2011, MNRAS, 410, 1096

Becker G. D., Hewett P. C., Worseck G., Prochaska J. X., 2013, MNRAS, 430, 2067

Birnboim Y., Dekel A., 2003, MNRAS, 345, 349

Bryan G. L. et al., 2014, ApJS, 211, 19

Chongchitnan S., Meiksin A., 2014, MNRAS, 437, 3639

Crighton N. H. M. et al., 2011, MNRAS, 414, 28

Croft R. A. C., 2004, ApJ, 610, 642

Dalla Vecchia C., Schaye J., 2008, MNRAS, 387, 1431

Dekel A., Birnboim Y., 2006, MNRAS, 368, 2

Dekel A., Silk J., 1986, ApJ, 303, 39

Faucher-Giguère C.-A., Kereš D., 2011, MNRAS, 412, L118

Faucher-Giguere C.-A., Hopkins P. F., Keres D., Muratov A. L., Quataert E., Murray N., 2015, MNRAS, 449, 987

Fumagalli M., Prochaska J. X., Kasen D., Dekel A., Ceverino D., Primack J. R., 2011, MNRAS, 418, 1796

Fumagalli M., Hennawi J. F., Prochaska J. X., Kasen D., Dekel A., Ceverino D., Primack J., 2014, ApJ, 780, 74

Genzel R. et al., 2011, ApJ, 733, 101

Goerdt T., Dekel A., Sternberg A., Gnat O., Ceverino D., 2012, MNRAS, 424, 2292

Haardt F., Madau P., 2012, ApJ, 746, 125

Haas M. R., Schaye J., Booth C. M., Dalla Vecchia C., Springel V., Theuns T., Wiersma R. P. C., 2013, MNRAS, 435, 2931

Harrison C. M., Alexander D. M., Mullaney J. R., Swinbank A. M., 2014, MNRAS, 441, 3306

Hennawi J. F. et al., 2006, ApJ, 651, 61

Hernquist L., Katz N., Weinberg D. H., Miralda-Escudé J., 1996, ApJ, 457, L51

Hinshaw G. et al., 2013, ApJS, 208, 19

Kay S. T., Pearce F. R., Jenkins A., Frenk C. S., White S. D. M., Thomas P. A., Couchman H. M. P., 2000, MNRAS, 316, 374

Kay S. T., Pearce F. R., Frenk C. S., Jenkins A., 2002, MNRAS, 330, 113

Kereš D., Katz N., Weinberg D. H., Davé R., 2005, MNRAS, 363, 2

Kirkman D., Tytler D., 2008, MNRAS, 391, 1457

Larson R. B., 1974, MNRAS, 169, 229

Lukić Z., Stark C. W., Nugent P., White M., Meiksin A. A., Almgren A., 2015, MNRAS, 446, 3697

Meiksin A. A., 2009, Rev. Mod. Phys., 81, 1405

Meiksin A., Bolton J. S., Tittley E. R., 2014, MNRAS, 445, 2462 (Paper I)

Miralda-Escudé J., 2005, ApJ, 620, L91

Nelson D., Genel S., Pillepich A., Vogelsberger M., Springel V., Hernquist L., 2015, preprint (arXiv:1503.02665)

Pandey K. L., Sethi S. K., 2013, ApJ, 762, 15

Prochaska J. X., Hennawi J. F., Simcoe R. A., 2013a, ApJ, 762, L19

Prochaska J. X. et al., 2013b, ApJ, 776, 136

Rahmati A., Pawlik A. H., Raicević M., Schaye J., 2013, MNRAS, 430, 2427

Rahmati A., Schaye J., Bower R. G., Crain R. A., Furlong M., Schaller M., Theuns T., 2015, MNRAS, 452, 2034

Rakic O., Schaye J., Steidel C. C., Rudie G. C., 2012, ApJ, 751, 94

Rakic O., Schaye J., Steidel C. C., Booth C. M., Dalla Vecchia C., Rudie G. C., 2013, MNRAS, 433, 3103

Rudie G. C. et al., 2012, ApJ, 750, 67

Schaye J., 2006, ApJ, 643, 59

Schaye J. et al., 2010, MNRAS, 402, 1536

Schaye J. et al., 2015, MNRAS, 446, 521

Scholz T. T., Walters H. R. J., 1991, ApJ, 380, 302

Shen S., Madau P., Guedes J., Mayer L., Prochaska J. X., Wadsley J., 2013, ApJ, 765, 89

Silk J., Djorgovski S., Wyse R. F. G., Bruzual A. G., 1986, ApJ, 307, 415

Springel V., 2005, MNRAS, 364, 1105

Springel V., Hernquist L., 2003, MNRAS, 339, 289 (SH03)

Steidel C. C., Erb D. K., Shapley A. E., Pettini M., Reddy N., Bogosavljević M., Rudie G. C., Rakic O., 2010, ApJ, 717, 289

Suresh J., Bird S., Vogelsberger M., Genel S., Torrey P., Sijacki D., Springel V., Hernquist L., 2015, MNRAS, 448, 895

Trainor R. F., Steidel C. C., 2012, ApJ, 752, 39

Tummuangpak P., Bielby R. M., Shanks T., Theuns T., Crighton N. H. M., Francke H., Infante L., 2014, MNRAS, 442, 2094

van de Voort F., Schaye J., Booth C. M., Dalla Vecchia C., 2011, MNRAS, 415, 2782

van de Voort F., Schaye J., Altay G., Theuns T., 2012, MNRAS, 421, 2809

Viel M., Haehnelt M. G., Springel V., 2004, MNRAS, 354, 684

Vogelsberger M. et al., 2014, MNRAS, 444, 1518

Weiner B. J. et al., 2009, ApJ, 692, 187

APPENDIX A: CONVERGENCE TESTS ON H I STATISTICS

The convergence of the fractional absorption excess δ_F with box size is tested in Fig. A1 using the ENZO simulations for a velocity window $\Delta v = 2000\,\mathrm{km\,s^{-1}}$ and a halo redshift uncertainty $\sigma_H = 520\,\mathrm{km\,s^{-1}}$, similar to the observations of Prochaska, Hennawi & Simcoe (2013a). Only small changes in δ_F, less than 0.02, are found for the gas around $\sim 10^{11.5}\,\mathrm{M_\odot}$ haloes. In the high-mass bin, there is considerable Poisson scatter in δ_F from the smaller box, in which there are only 14 haloes with $M_h > 10^{12}\,\mathrm{M_\odot}$.

We examine the possible role radiative transfer may have in the absorption features using the simplifying approximation of an attenuated radiation field within systems sufficiently dense to be
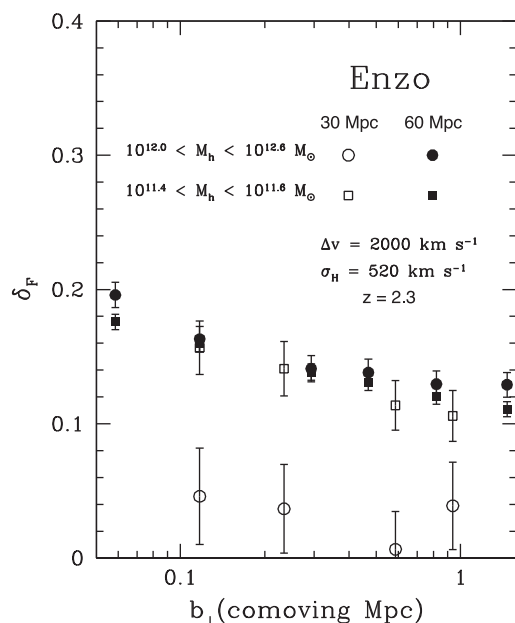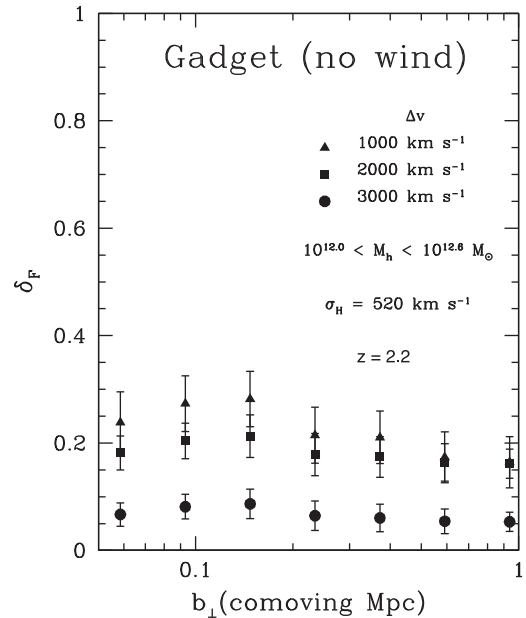

Figure A1. Fractional absorption excess δ_F relative to the mean IGM absorption for a velocity window $\Delta v = 2000\,\mathrm{km\,s^{-1}}$ around the halo centre-of-mass velocity. The data are shown as a function of the line-of-sight impact parameter $b_\perp$ for halo masses $11.4 < \log_{10} M_h = 11.6$ (squares) and $12.0 < \log_{10} M_h < 12.6$ (circles) at $z = 2.3$, for the ENZO simulations in boxes of side 30 Mpc (E30_1024, open symbols) and 60 Mpc (E60_1024, filled symbols). While the predictions converge well for moderate-mass haloes, differences arise for the most massive haloes, although the uncertainties are large because of the small number of haloes in the 30 Mpc box. Halo velocities include a random component drawn from a Gaussian distribution with standard deviation $\sigma_H = 520\,\mathrm{km\,s^{-1}}$.
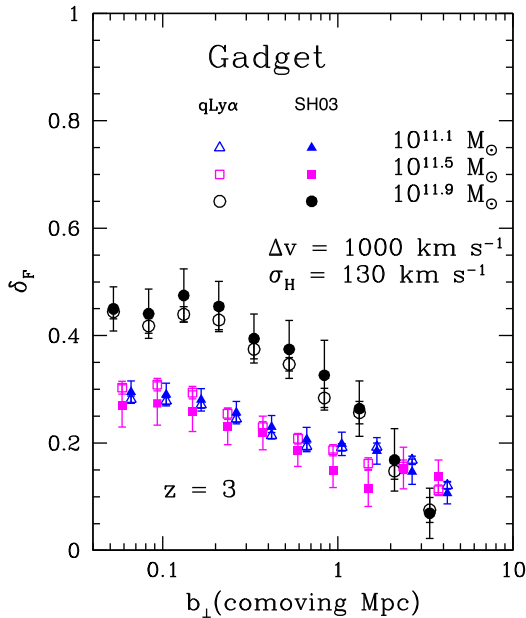
Figure A2. Fractional absorption excess δ_F relative to the mean IGM absorption within a $\Delta v = 1000\,\mathrm{km\,s^{-1}}$ window centred on the halo centre-of-mass velocity. The data are shown as a function of the line-of-sight impact parameter $b_\perp$ for halo masses $\log_{10} M_h = 11.1$ (triangles; blue), 11.5 (squares; magenta) and 11.9 (circles; black) at redshift $z = 3$, for the GADGET-3 non-wind simulations using the default star formation prescription of SH03 (G39sfnw, filled symbols) or quick Lyα (G30qLyα open symbols). The choice of gas removal algorithm has little impact on the amount of absorption. Halo velocities include a random component drawn from a Gaussian distribution with standard deviation $\sigma_H = 130\,\mathrm{km\,s^{-1}}$.

Figure A3. Fractional absorption excess δ_F relative to the mean IGM for halo masses $12.0 < \log_{10} M_h < 12.6$ within velocity windows of width $\Delta v = 1000\,\mathrm{km\,s^{-1}}$ (triangles), $2000\,\mathrm{km\,s^{-1}}$ (squares) and $3000\,\mathrm{km\,s^{-1}}$ (circles). The results are centred on the halo centre-of-mass velocity as a function of the line-of-sight impact parameter $b_\perp$ for the GADGET-3 non-wind simulations (G30sfnw) at $z = 2.2$. While increasing the velocity window reduces the variance, it also suppresses the signal. The window $\Delta v = 2000\,\mathrm{km\,s^{-1}}$ is a good compromise. Halo velocities include a random component drawn from a Gaussian distribution with standard deviation $\sigma_H = 520\,\mathrm{km\,s^{-1}}$.

self-shielding to photoionizing radiation. We adopt the prescription of Rahmati et al. (2013), using a characteristic self-shielding total hydrogen density of $0.0064T_4^{0.17}\,\mathrm{cm^{-3}}$ for temperature $T_4 = T/10^4\,\mathrm{K}$. Rahmati et al. (2013) find wide scatter about the mean correction. We find that the effect on the mean values of δ_F, however, is under 5 per cent, and generally less than 1 per cent. We therefore neglect the effects of radiative transfer in this paper on the integrated amount of absorption. Radiative transfer does of course affect the column densities of optically thick discrete absorption systems, and so must be included when examining their statistics. The presence of any local sources of photoionizing radiation would further modify the neutral fractions and gas temperatures. Since we cannot include the physical response of the gas due to the resulting temperature and consequent internal pressure changes these systems would undergo, especially important for those largely neutral, having $N_{H\,I} > 10^{19}\,\mathrm{cm^{-2}}$, or to the presence of any local ionizing sources, we do not consider such high column density systems except for their small contribution to the statistics for column density thresholds we do examine, $N_{H\,I} > 10^{16}\,\mathrm{cm^{-2}}$ and $N_{H\,I} > 10^{17.3}\,\mathrm{cm^{-2}}$ in Fig. 7. The effects of radiative transfer are included for these systems. We have also compared results for δ_F using Doppler and Voigt profile functions for run G30sfnw. The differences were negligible. We use the Doppler profile function for the results presented here since it requires an order of magnitude less analysis time. The Voigt function was used, however, when including the effects of radiative transfer.

All the GADGET-3 simulations for the results in this paper use the star formation prescription of SH03. In Fig. A2, we compare the results for δ_F using the quick Lyα method instead. Very little difference is found, suggesting that the results are robust to the method of gas removal.

Increasing the velocity window width Δv suppresses the values of δ_F at all impact parameters within the turnaround radius of massive haloes, while reducing the spread in values, as shown in Fig. A3. Decreasing Δv from 2000 to $1000\,\mathrm{km\,s^{-1}}$ slightly increases the signal while producing a somewhat wider spread. A window width of $\Delta v = 2000\,\mathrm{km\,s^{-1}}$ produces a good compromise between these competing effects. Velocity window widths $\Delta v = 1000$ and $2000\,\mathrm{km\,s^{-1}}$ to compute δ_F are used by Rakic et al. (2012) and Prochaska et al. (2013b), respectively, much wider than the respective typical halo velocity errors of $\sigma_H = 130$ and $520\,\mathrm{km\,s^{-1}}$. We have confirmed that a halo velocity uncertainty as large as half the velocity window affects the values of δ_F by less than 2 per cent.

Finally, the relative fluctuations in the Lyα flux in a given velocity window in random diffuse IGM regions increase with redshift. In Fig. A4, we show the convergence in our simulations to the IGM data measured in a spectral window of $\Delta v = 2000\,\mathrm{km\,s^{-1}}$ (Prochaska et al. 2013b) for large impact parameters around the haloes. The diffuse IGM value is approached most rapidly in the gaseous surroundings of the lower mass haloes, for which the mesogalactic region is smaller.
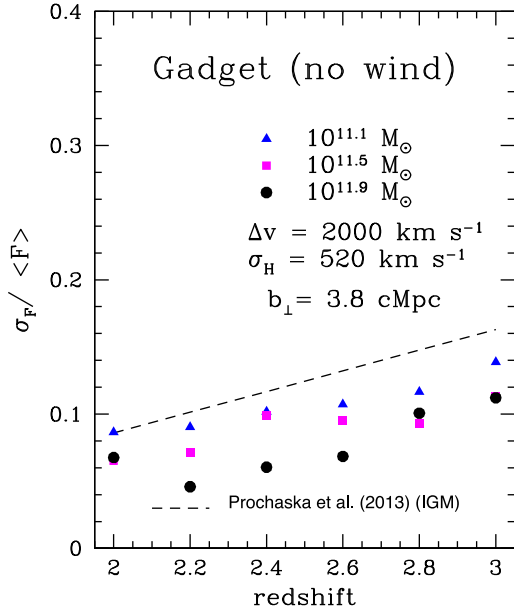
Figure A4. Relative flux fluctuation $\sigma_F/\langle F \rangle$ averaged over a velocity window $\Delta v = 2000\,\mathrm{km\,s^{-1}}$ centred on the halo centre-of-mass velocity for halo masses $\log_{10} M_h = 11.1$ (triangles; blue), 11.5 (squares; magenta) and 11.9 (circles; black) at $b_\perp = 3.8$ Mpc (comoving). The results are displayed as a function of redshift for the GADGET-3 non-wind simulation (G30sfnw). The dashed line is the fit from Prochaska et al. (2013b) to IGM measurements. It is most closely approached for the lower mass haloes. Halo velocities include a random component drawn from a Gaussian distribution with standard deviation $\sigma_H = 520\,\mathrm{km\,s^{-1}}$.

This paper has been typeset from a TEX/LATEX file prepared by the author.